Determination of the direct capture contribution for $^{13}N(p,\gamma)^{14}O$ from the $^{14}O \rightarrow {}^{13}N+p$ asymptotic normalization coefficient

Xiaodong Tang*

Cyclotron Institute, Texas A&M University, College Station, Texas 77843, USA
and Physics Division, Argonne National Laboratory, Argonne, Illinois 60439, USA

A. Azhari, Changbo Fu, C. A. Gagliardi, A. M Mukhamedzhanov, F. Pirlepesov, L. Trache, and R. E. Tribble
Cyclotron Institute, Texas A&M University, College Station, Texas 77843, USA

V. Burjan and V. Kroha
Institute of Nuclear Physics, Czech Academy of Sciences, Prague-Řež, Czech Republic

F. Carstoiu
Institute of Physics and Nuclear Engineering H. Hulubei, Bucharest, Romania

B. F. Irgaziev
Department of Physics, National University, Tashkent, Uzbekistan

$^{13}N(p,\gamma)^{14}O$ is one of the key reactions which trigger the onset of the hot CNO cycle. This transition occurs when the proton capture rate on ^{13}N is faster, due to increasing stellar temperature ($\geqslant 10^8$ K), than the ^{13}N β-decay rate. The rate of this reaction is dominated by the resonant capture through the first excited state of ^{14}O ($E_r=0.528$ MeV). However, through constructive interference, direct capture below the resonance makes a non-negligible contribution to the reaction rate. We have determined this direct contribution by measuring the asymptotic normalization coefficient for $^{14}O \rightarrow {}^{13}N+p$. In our experiment, an 11.8 MeV/nucleon ^{13}N radioactive beam was used to study the $^{14}N(^{13}N,^{14}O)^{13}C$ peripheral transfer reaction, and the asymptotic normalization coefficient, $(C_{p_{1/2}}^{^{14}O})^2 = 29.0 \pm 4.3$ fm^{-1}, was extracted from the measured cross section. The radiative capture cross section was estimated using an R-matrix approach with the measured asymptotic normalization coefficient and the latest resonance parameters. We find the S factor for $^{13}N(p,\gamma)^{14}O$ to be larger than previous estimates. Consequently, the transition from the cold to hot CNO cycle for novae would be controlled by the slowest proton capture reaction $^{14}N(p,\gamma)^{15}O$.

I. INTRODUCTION

The nova is one of most violent observable events to occur in the Universe. It is believed to happen when a white dwarf in an accreting binary system acquires a hydrogen-rich envelope from its companion star. The subsequent hydrogen ignition may take place under degenerate conditions and therefore lead to an explosion. Hydrodynamic calculations show that this scenario occurs at temperatures in the range $0.1 < T_9 < 0.3$, where T_9 is the temperature in units of 10^9 K. At lower temperatures, the cold CNO cycle operates and the energy generation rate is dominated by the slowest proton capture reaction, $^{14}N(p,\gamma)^{15}O$. The energy generation rate of the cold CNO cycle can be approximated by multiplying the $^{14}N(p,\gamma)^{15}O$ reaction rate with the energy release from fusion,

$$\epsilon_{CNO} = \frac{4.5 \times 10^{25}\rho X_H Z_{CNO}}{T_9^{2/3}} e^{-15.228/T_9^{1/3}} (\text{erg g}^{-1}\text{s}^{-1}), \quad (1)$$

where Z_{CNO} is the mass fraction of the CNO material, X_H is the mass fraction of the hydrogen, and ρ is the density in g/cm^3 [1]. In Eq. (1), it has been assumed that about 50% of the CNO material is stored as ^{14}N.

With increasing temperature, the rates of the proton capture reactions in the cold CNO cycle exponentially increase. Eventually the reaction rate for $^{13}N(p,\gamma)^{14}O$ exceeds the rate of ^{13}N β decay ($t_{1/2}=9.965$ min) and the hot (β-limited) CNO cycle takes over as shown in Fig. 1. But $^{14}N(p,\gamma)^{15}O$ is still the slowest reaction and it controls the energy generation rate. As the temperature continues to increase, all of the proton capture reaction rates in the hot CNO cycle exceed the β-decay rates of ^{14}O and ^{15}O (with half-lives $t_{1/2} = 70.6$ s and 122 s, respectively). Therefore, the energy generation rate of the hot CNO cycle is approximately a constant,

$$\epsilon_{HCNO} = 4.6 \times 10^{15} Z_{CNO} (\text{erg g}^{-1}\text{s}^{-1}). \quad (2)$$

In Eq. (2), about 50% of the CNO material is assumed to be stored as ^{14}O and ^{15}O [1]. The energy generation rate of the hot CNO cycle will remain constant until some breakout processes begin to occur. The thermonuclear runaway in no-

---

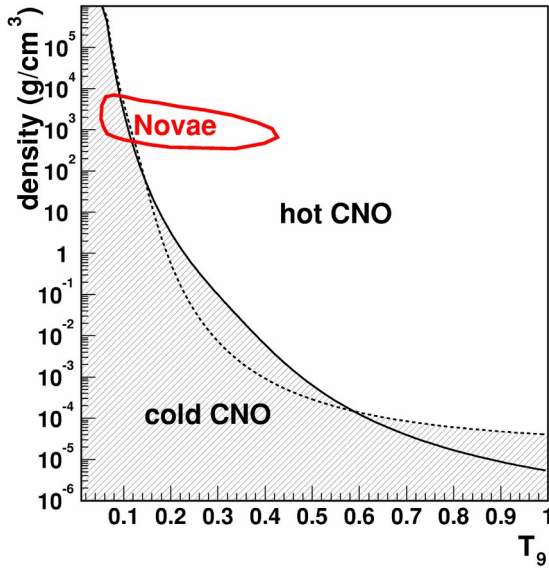*Electronic address: xdtang@phy.anl.gov

FIG. 1. (Color online) Density and temperature conditions for the transition from the cold to hot CNO cycle for a typical novae hydrogen mass fraction $X_H=0.77$. The solid line is the calculation with the competition between $^{13}N(p,\gamma)^{14}O$ and the β decay of ^{14}O and ^{15}O. The dashed line is the calculation with the competition between $^{14}N(p,\gamma)^{15}O$ and the β decay of ^{14}O and ^{15}O. The hot CNO cycle operates in the upper unshaded region. The typical temperature and density condition for novae [1] is also shown as the circle in the upper left corner. The rates used in the calculation are taken from NACRE [3].

FIG. 2. Low-lying energy levels of ^{14}O and the two *s*-wave radiative capture processes in $^{13}N(p,\gamma)^{14}O$. Because both processes involve E1 transitions, they interfere.

vae is driven by the energy release of the hot CNO cycle. Because the peak temperature in the thermonuclear runaway is typically below 3.5×10^8 K, breakout processes are inhibited by their limited reaction rates. Observation of the abundance distribution in nova ejecta indicates large overabundances of nitrogen produced by the β decay of the bottleneck nuclei, ^{14}O and ^{15}O, in the hot CNO cycle [1].

As shown in Eqs. (1) and (2), a rapid change in the energy generation rate occurs once the CNO cycle transits from cold to hot. This transition condition, which is a function of temperature and density, can be determined by finding when the rates between the β decay of ^{14}O and ^{15}O and the slowest proton capture reaction in the cycle are equal. This is shown in Fig. 1 and given by [2]

$$\rho = 1.0/[(\tau_{14} + \tau_{15})X_H(N_A\langle\sigma v\rangle_{min})], \qquad (3)$$

where τ_{14} and τ_{15} are the lifetimes of ^{14}O and ^{15}O, respectively, X_H is the mass fraction of hydrogen, and $N_A\langle\sigma v\rangle_{min}$ is the smallest proton capture reaction rate in the hot CNO cycle. For temperatures less than $T_9=0.14$, the $^{14}N(p,\gamma)^{15}O$ reaction rate is slightly slower than the $^{13}N(p,\gamma)^{14}O$ rate. Thus the $^{14}N(p,\gamma)^{15}O$ reaction controls the transition from the cold to hot CNO cycle. A recent result from $^{14}N(^3He,d)^{15}O$ [4,5] shows that NACRE overestimated the

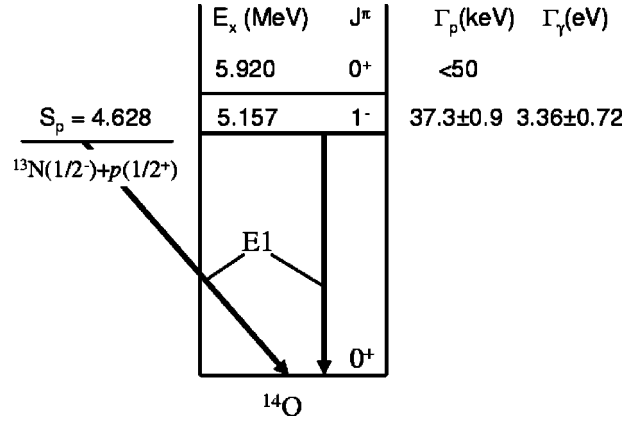$^{14}N(p,\gamma)^{15}O$ rate by 54–84 % for $T_9<0.1$. This further solidifies the importance of $^{14}N(p,\gamma)^{15}O$ in the cold CNO cycle and the transition from the cold to hot CNO cycle with $T_9<0.1$. For temperatures from $T_9=0.14$ to $T_9=0.59$, the $^{13}N(p,\gamma)^{14}O$ reaction rate is the slowest and it completely dominates this transition. Therefore, precise determinations of the rates for these capture reactions are vital for predicting the conditions where the transition from the cold to hot CNO cycle occurs.

For $T_9=0.2$, the Gamow window for the $^{13}N(p,\gamma)^{14}O$ reaction is located at 148 keV with a width of 117 keV. At this energy, the reaction is dominated by the low-energy tail of the *s*-wave capture on the broad 1^- resonance at $E_r=0.529$ MeV, which has a total width of 37.3 ± 0.9 keV (see Fig. 2). The direct capture contribution is significantly smaller than that due to the tail of the resonance within the Gamow window. But since both resonant and nonresonant capture proceed via *s* waves and then decay by E1 transitions, there is an interference between the two components. Thus the resonant tail can be enhanced through constructive interference or reduced through destructive interference. Previously Decrock *et al.* [6] used the $^{13}N(d,n)^{14}O$ reaction to determine the spectroscopic factor of 0.90 ± 0.23, from which they then obtained the direct capture contribution to the reaction rate. Based on their result, direct capture yields a nonnegligible contribution to the reaction rate at low energy.

It is well known that direct capture is proportional to the asymptotic normalization of the tail of the bound state overlap integral and that this quantity can be determined by peripheral proton transfer reactions [7]. We have used the peripheral transfer reaction $^{14}N(^{13}N,^{14}O)^{13}C$ at 11.8 MeV/nucleon to measure the asymptotic normalization coefficient (ANC) for $^{14}O\rightarrow^{13}N+p$, thus yielding a more precise determination of the nonresonant capture cross section. The capture rate for $^{13}N(p,\gamma)^{14}O$ has then been determined from the measured ANC and the latest parameters available for the resonance states using an R-matrix analysis similar to that described in a previous paper [8].

II. EXPERIMENTAL PROCEDURE

The ^{13}N radioactive beam was produced via the $^1H(^{13}C,^{13}N)n$ reaction using a ^{13}C beam of $\sim$600 enA at

15 MeV/nucleon from the K500 superconducting cyclotron at Texas A&M University. The beam bombarded a 10-cm-long, LN$_2$-cooled, cryogenic H$_2$ gas cell with 12.7 μm Havar windows. ^{13}N recoils at 11.8 MeV/nucleon were collected by the Momentum Achromat Recoil Spectrometer (MARS) at 0°. They were separated from the primary beam and other reaction products and focused on a secondary target. For beam studies, a 5×5 cm, 1000-μm-thick, position-sensitive silicon detector was mounted on the secondary target ladder. The detector consisted of 16 3-mm-wide resistive strips on one side that provided for both vertical and horizontal position measurements. The vertical position resolution along the resistive strips was better than 1 mm [full width at half maximum (FWHM)]. The total energy deposited in the detector was provided by a read-out on the back plane. After tuning MARS, the secondary beam spot size and divergence were measured to be 3 mm (FWHM) and 1.8° (FW) in x and 3.2 mm (FWHM) and 1.9° (FW) in y. The energy spread of the beam was set to 1.6 MeV. The purity was better than 99%, with the primary contaminant being ^{11}C. Secondary beam rates on target were typically over 600 kHz. For a detailed description of radioactive beam production with MARS, see Ref. [9].

A secondary reaction target consisted of 1.5 mg/cm^2 melamine (C$_3$N$_6$H$_6$) on 20 μg/cm^2 C and 20 μg/cm^2 collodion backings. The thickness and uniformity were verified by direct measurements with the ^{13}N beam by observing the beam energy spectrum with and without the target. With a peak shift of 2.46 MeV, the dE/dx calculation from the ion-beam–target interaction program SRIM [10] gave the central target thickness to be 1.48 mg/cm^2 with an uncertainty of 6%, arising from the SRIM calculation and the statistical uncertainty from the peak shift. Reactions were also observed from a ^{12}C target of 1.9 mg/cm^2 in order to obtain elastic scattering data and to verify that no peaks from the C in the melamine target interfered with the transfer reactions of interest from ^{14}N.

The reaction products from the ^{13}N secondary beam bombarding the two separate targets were recorded by two detector telescopes, each of which consisted of a 5×5 cm 16-strip position-sensitive Si detector, with a thickness of 60 μm, backed by a 500 μm Si detector. The telescopes were separated from the target by a distance of 200 mm. Both telescopes were cooled to $-6\,°$C to reduce thermal noise. In order to avoid beam hitting the detectors and to reduce the yield from small angle elastic scattering, the two telescopes were separated by 28 mm. A NE102A plastic scintillator coupled to a photomultiplier tube by a lucite light guide was mounted between the two Si telescopes to monitor the ^{13}N beam. Since the full beam intensity was too high for the scintillator, two screens, each with a transparency of 9%, were added to attenuate the beam intensity. The total effective transparency, 1.5%, was measured in special runs that compared the ^{13}N yield observed in the target detector and the plastic scintillator detector for equal ^{13}C incident beam intensities. Details of the detector setup can be found in a previous publication [8].
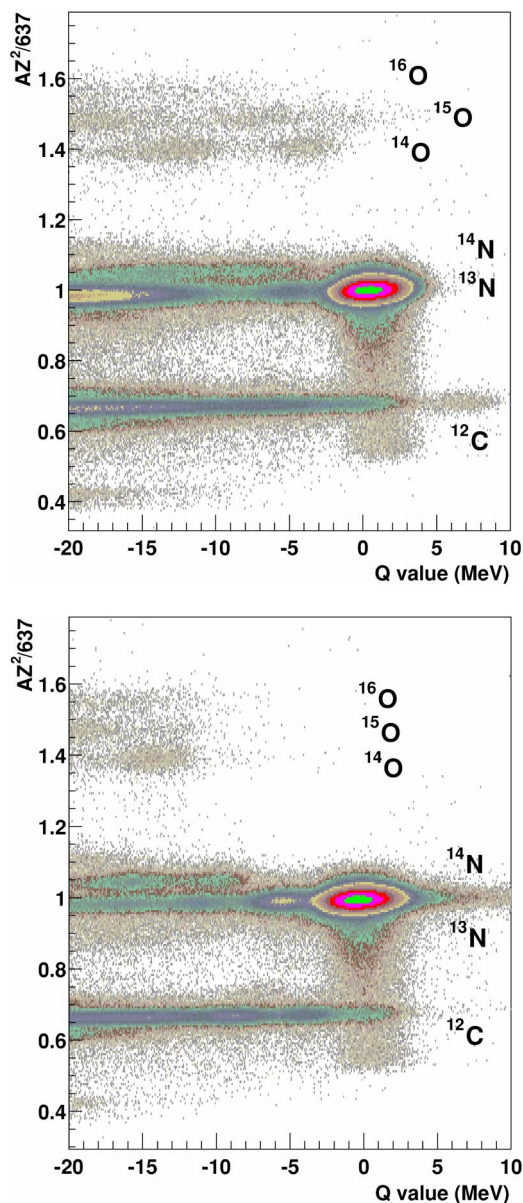

FIG. 3. (Color online) The particle identification vs Q-value distribution from the melamine (top panel) and C (bottom panel) targets. The ^{13}N group with Q value of 0 MeV is the elastic scattering off the C and N in the melamine target. There was a small Ta contaminant in the C foil that appears as a tail to positive Q value. In the spectrum from the melamine target, the broad peak with a Q value of about -20 MeV is due to elastic scattering off H and the least negative Q value peak in ^{14}O is from ^{14}N$(^{13}$N$,^{14}$O$)^{13}$C$_{g.s.}$.

III. DATA ANALYSIS

After calibrating the energy and position outputs for the two telescopes, a particle identification, based on the energy loss in the ΔE detector and the total energy loss, and reconstructed Q value were calculated from the experimental data as described in a previous paper [8]. The result from the melamine target is shown in the top panel of Fig. 3. The ^{13}N elastic scattering can be easily identified as the group with large yield at zero Q value. Elastic scattering occurs on ^{14}N, ^{12}C, and ^{1}H nuclei in melamine. Due to the inverse kinemat-

ics, the maximum allowed laboratory scattering angle for $^1H(^{13}N, ^{13}N)^1H$ is $5.22°$ and the kinematic shift of the ^{13}N recoils is large near the maximum angle. The detector system covered lab angles from $4°$ to $17°$, so scattering from ^1H was easily separated from $^{14}N(^{13}N, ^{13}N)^{14}N$. The other two elastic scattering reactions, $^{14}N(^{13}N, ^{13}N)^{14}N$ and $^{12}C(^{13}N, ^{13}N)^{12}C$, were indistinguishable at small angles due to the finite energy spread of the ^{13}N beam. During the analysis, a manual cut was set on the energy versus angle spectrum to accept both elastic processes, independent of scattering angle.

The first excited states of ^{13}N, ^{14}N, and ^{12}C are at 2.37 MeV, 2.31 MeV, and 4.44 MeV, respectively. The transition between the ground state of ^{14}N and the first excited state is a pure $M1$ transition. Inelastic excitation of this state was found to be weak in a previous study of $^{13}C(^{14}N, ^{14}N)^{13}C$ at a similar energy [11], and it also is expected to be weak in the present case. Inelastic excitation of the first excited state in ^{12}C occurs via a collective $E2$ transition. It was a strong inelastic process in our experiment and appears as a ^{13}N peak with a Q value around -5 MeV in Fig. 3. The shift in the Q value from the actual energy of -4.44 MeV is due to the assumption, during analysis, that scattering occurred off of ^{14}N. The first excited state of ^{13}N is proton unbound and thus inelastic excitation to it does not appear in the ^{13}N group. The particle identification versus Q-value spectrum for ^{12}C is shown in the bottom panel of Fig. 3. By comparing the two spectra, it is obvious that all the reaction channels relating to ^{14}N and ^1H disappear. Due to a trace amount of Ta contamination, a higher-energy ^{13}N recoil branch was observed in the total energy versus angle spectrum for the elastic channel. The amount of Ta was determined by comparing the cross section with Rutherford scattering.

The Q-value spectrum for ^{14}O particles from reactions between ^{13}N and the melamine target is shown together with the same Q-value spectrum for reactions on the ^{12}C target in Fig. 4. No bound excited states of ^{14}O exist, so only proton transfer reactions leading to the ground state could be observed. The least negative Q-value peak corresponds to the $^{14}N(^{13}N, ^{14}O)^{13}C_{g.s.}$ reaction. The small peak with a Q value around -7 MeV is due to reactions leading to excited states of ^{13}C. The peak at a Q value of -12 MeV is mainly from the $^{12}C(^{13}N, ^{14}O)^{11}B_{g.s.}$ reaction. This was verified by the results from the ^{12}C target which are shown as the dashed line in Fig. 4. The transfer reaction on ^{12}C contributes about 70% of the yield in this region. The additional 30% of the yield comes from transfer reactions leading to excited states of ^{13}C.

During the data analysis to obtain the transfer reaction angular distribution, a manual cut was set on the particle identification versus Q-value spectrum to select the transfer reaction events of interest. Due to the large beam energy spread, there is some overlap between the ^{14}O peak due to transitions to the ^{13}C ground state and excited states. To estimate this background contribution, Monte Carlo simulations were used to reproduce the two peaks. From the simulation we find that a Q-value cut at -5.63 MeV will accept 97% of the events of interest with a 3.4% contamination
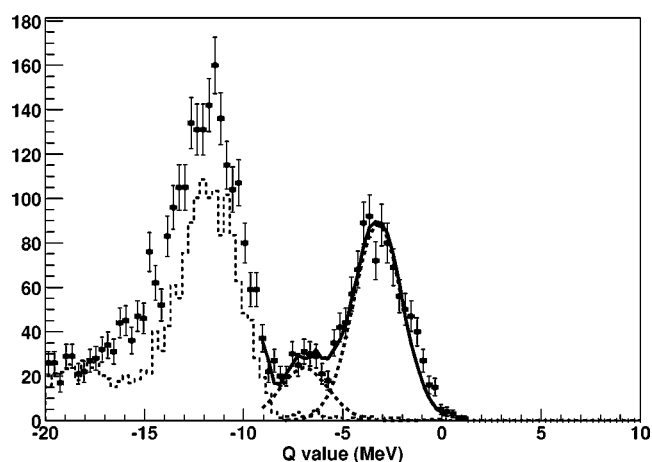

FIG. 4. Q-value spectrum for ^{14}O reaction products. The peak at -3.0 MeV is from the $^{14}N(^{13}N, ^{14}O)^{13}C_{g.s.}$ reaction. The peak near -7 MeV reflects population of ^{13}C excited states. The peak at -12 MeV is mainly from the $^{12}C(^{13}N, ^{14}O)^{11}B_{g.s.}$ reaction. After subtracting the contribution from ^{12}C, which is obtained from the runs with the ^{12}C target and is shown as the dashed peak located around -12 MeV, the ^{13}N induced proton transfer reactions on ^{14}N in the melamine target were fit with the simulation results. This is shown as the two dashed peaks located around -3 MeV and -7 MeV, respectively. The sum of these three contributions is shown as the solid line.

from proton transfer reactions leading to the excited states of ^{13}C. The amount of contamination grows to about 8% with a Q-value cut at -6.30 MeV. Therefore, the error from setting this threshold was conservatively estimated as $\pm 5\%$.

IV. ELASTIC SCATTERING AND OPTICAL-MODEL POTENTIALS

The experimental elastic scattering cross section for ^{13}N on the melamine target is shown in Fig. 5 together with an optical-model calculation. The calculation has been smoothed to account for finite angular acceptance. Since we cannot distinguish between the elastic scattering of ^{13}N off of ^{14}N or ^{12}C in the melamine target, the two reaction channels were summed together in the laboratory scattering frame according to their atomic ratios, then the combined result was converted to the center-of-mass frame using the kinematics appropriate for $^{13}N + ^{14}N$. The optical-model parameters were obtained from double-folding-model calculations [12]. The parameter sets for the tightly bound nuclei were chosen in the calculation for ^{13}N elastic scattering off of the melamine target [8]. The forward angle cross section, which is dominated by Coulomb scattering, is not very sensitive to the optical-model parameters. Varying the normalization factors for the $^{13}N + ^{12}C$ and $^{13}N + ^{14}N$ real and imaginary potentials within their uncertainties, as in Ref. [12], only resulted in a 1.2% change in the elastic scattering cross section for these angles. Therefore, this region is used to examine the absolute normalization. A comparison between the first three experimental data points and the smeared prediction shown in Fig. 5 shows that they agree to within $8 \pm 4\%$, which is consistent with the our estimate for the uncertainty arising from the
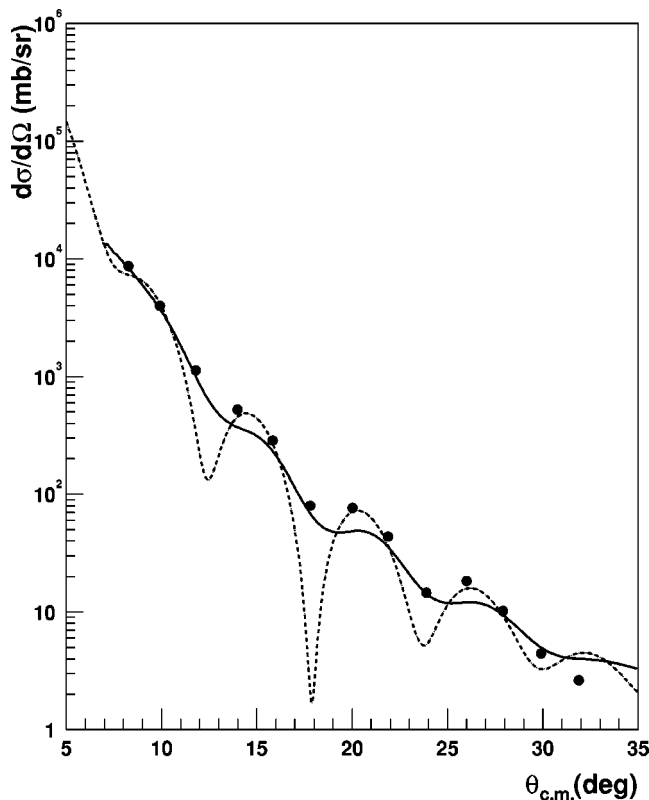
FIG. 5. Elastic scattering angular distributions for ^{13}N on melamine. The experimental results are shown as dots. The statistical uncertainty is smaller than the size of the data points. There is an additional 6.5% normalization uncertainty that is common for all the data points. The dashed curve is the summed prediction for ^{13}N elastic scattering off of C and N in the melamine target. The solid curve is the smeared result for the prediction.
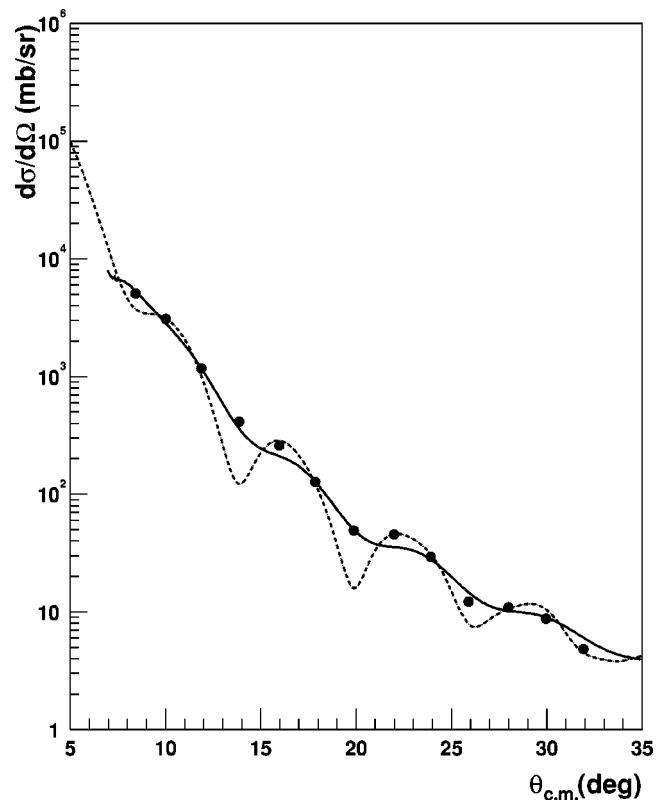

FIG. 6. Elastic scattering angular distributions for ^{13}N on ^{12}C. The contribution from Ta contamination in the ^{12}C target is added to the ^{13}N scattering off ^{12}C assuming it to be pure Rutherford scattering. The experimental results are shown as dots. The statistical uncertainty is smaller than the size of the data points. There is an additional 6.5% normalization uncertainty that is common for all the data points. The dashed curve is the summed prediction for ^{13}N elastic scattering off C and Ta in the ^{12}C target. The solid curve is the smeared result for the prediction.

incident beam normalization and target thickness.

The experimental elastic scattering cross section for ^{13}N on the ^{12}C target was also measured and is shown in Fig. 6. These data provide an independent check on the optical model prediction for ^{12}C in the melamine target. The comparison between the first three experimental data points and the smeared prediction in Fig. 6 shows that they agree to within $1\pm7\%$.

V. ^{14}N(^{13}N, ^{14}O)^{13}C ANGULAR DISTRIBUTION AND THE ANC FOR ^{14}O $\rightarrow$ ^{13}N+p

The angular distribution for the ^{14}N(^{13}N, ^{14}O)^{13}C reaction is shown in Fig. 7. The solid curve is a distorted wave Born approximation (DWBA) prediction for the proton transfer reaction that uses the tightly bound optical-model parameters for ^{13}N+^{14}N and the loosely bound parameters for ^{14}O+^{13}C [12]. The ANCs for ^{14}N $\rightarrow$ ^{13}C+p were determined to be $C^2_{p_{1/2}}=18.2\pm0.9$ fm^{-1} and $C^2_{p_{3/2}}=0.91\pm0.14$ fm^{-1} in previous studies of ^{13}C(^{14}N, ^{13}C)^{14}N [11] and ^{13}C(^{3}He, d)^{14}N [13].

By normalizing the predictions to the experimental data [14],

$$\sigma_{\text{exp}} = (C^{^{14}\text{O}}_{p_{1/2}})^2 \left[\left(\frac{C^{^{14}\text{N}}_{p_{1/2}}}{b^{^{14}\text{O}}_{p_{1/2}} b^{^{14}\text{N}}_{p_{1/2}}} \right)^2 \sigma^{\text{DW}}_{p_{1/2}, p_{1/2}} \right.$$
$$\left. + \left(\frac{C^{^{14}\text{N}}_{p_{3/2}}}{b^{^{14}\text{O}}_{p_{1/2}} b^{^{14}\text{N}}_{p_{3/2}}} \right)^2 \sigma^{\text{DW}}_{p_{1/2}, p_{3/2}} \right], \quad (4)$$

the value of the ANC for ^{14}O $\leftrightarrow$ ^{13}N+p was found to be $C^2_{p_{1/2}}=29.0\pm4.3$ fm^{-1}. The b's in the equation are the single-particle ANCs assumed in the DWBA calculations for the two different transfers. The uncertainties for σ_{exp} in Eq. (4) include statistics (3.0%), absolute normalization of the cross section (7%), and the error from setting the Q-value threshold (5%). The uncertainties contributed by the inputs to the Monte Carlo simulation were investigated by varying the beam center within its uncertainty and rotating the angle of the detectors within 1°. The overall uncertainty from these effects is 2.0%. By changing the normalization constants of the real and imaginary optical potentials for the incoming and outgoing channels within their uncertainties from Ref. [12], the variation of the DWBA calculations was found to
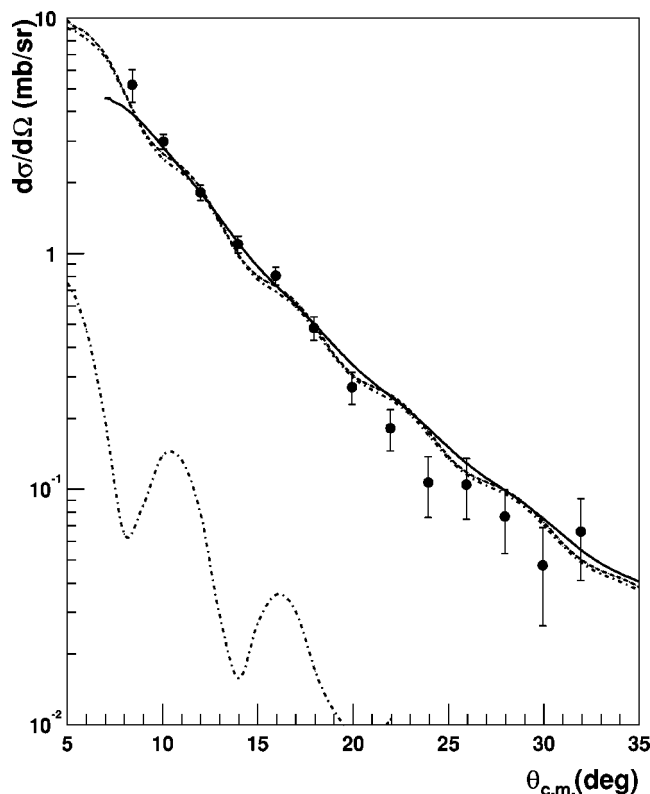
FIG. 7. Transfer reaction angular distributions for $^{14}\text{N}(^{13}\text{N},{}^{14}\text{O})^{13}\text{C}_{\text{g.s.}}$. The dashed curve is the DWBA prediction. The solid curve is the smeared prediction. The ANC was found by normalizing this curve to the experimental data. The two dashed-dotted curves show the separate angular momentum contributions from Eq. (4), before correcting for finite angular resolution. The upper and lower lines represent the $^{14}\text{N}(p_{1/2}) \rightarrow {}^{14}\text{O}(p_{1/2})$ and $^{14}\text{N}(p_{3/2}) \rightarrow {}^{14}\text{O}(p_{1/2})$ proton transfer reactions, respectively.

be less than 8.0%. A comparison of the DWBA calculations from PTOLEMY [15] and Fresco [16] shows that they agree to 5% for $\theta_{\text{c.m.}} < 30°$. The knowledge of the $^{14}\text{N} \leftrightarrow {}^{13}\text{C}+p$ ANCs introduced an uncertainty of 6.4%. Combining these gives a total uncertainty of 14.7%.

VI. S FACTOR FOR $^{13}\text{N}(p,\gamma)^{14}\text{O}$

The cross section for direct and resonant capture through the broad first excited state can be calculated from the measured ANC and the experimental resonance parameters using the R-matrix approach [8]. In the calculation, the same parameters ($E_R^{\text{c.m.}} = 527.9 \pm 1.7$ keV, $\Gamma_{\text{total}} = 37.3 \pm 0.9$ keV, and $\Gamma_\gamma = 3.36 \pm 0.72$ eV) as Magnus *et al.* [17] adopted were used for the first resonance. What is not known is the sign of the interference term between the two components.

It is possible to sometimes infer the sign of the interference to be used in an R-matrix calculation of the radiative capture cross section even in the absence of direct experimental data [8,18]. Such is the case for the reaction being considered here. The resonant amplitude can be separated into an internal and channel (external) part [8,18]. At energies below the resonance, the channel part, which depends
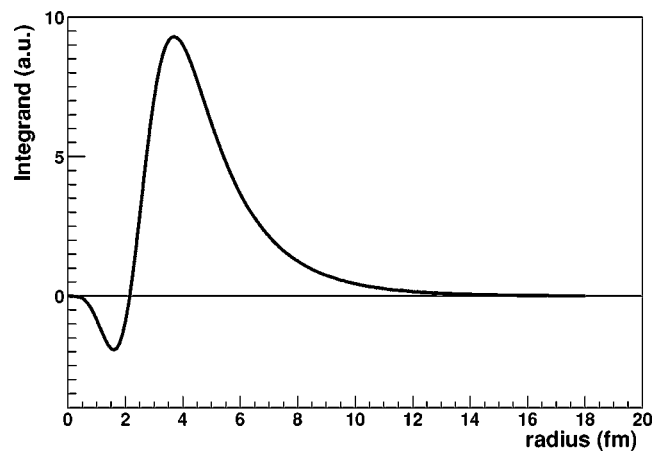

FIG. 8. The integrand of the $E1$ transition matrix element based on a single-particle model at resonant energy.

on the ANC [8], has the same sign as the nonresonant amplitude leading to constructive interference for these two terms. From the equations given in [8,19], $[\Gamma_{\gamma J_f}^{J_i}(E_R^{\text{c.m.}})]_{\text{ch}}^{1/2} = 0.90 + i\,0.02$ eV$^{1/2}$ and the channel radiative width $|[\Gamma_{\gamma J_f}^{J_i}(E_R^{\text{c.m.}})]_{\text{ch}}| = 0.81$ eV for a channel radius $a = 5$ fm. The total resonance radiative width is $\Gamma_\gamma(E_R^{\text{c.m.}}) = |[\Gamma_{\gamma J_f}^{J_i}(E_R^{\text{c.m.}})]_{\text{int}}^{1/2} + [\Gamma_{\gamma J_f}^{J_i}(E_R^{\text{c.m.}})]_{\text{ch}}^{1/2}|^2$. Thus there are two possible solutions for the internal part, a large negative value $[\Gamma_{\gamma J_f}^{J_i}(E_R^{\text{c.m.}})]_{\text{int}(1)}^{1/2} = -2.73$ eV$^{1/2}$ and a small positive value $[\Gamma_{\gamma J_f}^{J_i}(E_R^{\text{c.m.}})]_{\text{int}(2)}^{1/2}$
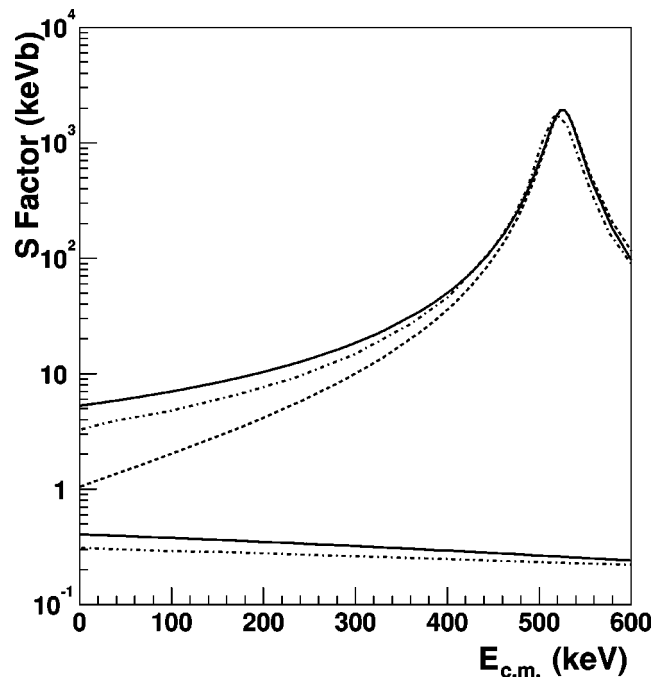
FIG. 9. S factor for $^{13}\text{N}(p,\gamma)^{14}\text{O}$. The relatively flat solid line is the direct capture contribution determined from the ANC. This result is higher than that obtained by Decrock *et al.* (lowest dash-dotted line). Based on constructive interference, our updated result for the total S factor, the top solid line, is about 38% higher than the previous result (upper dash-dotted line). For completeness, we show the result that would be obtained with destructive interference as the dashed line.
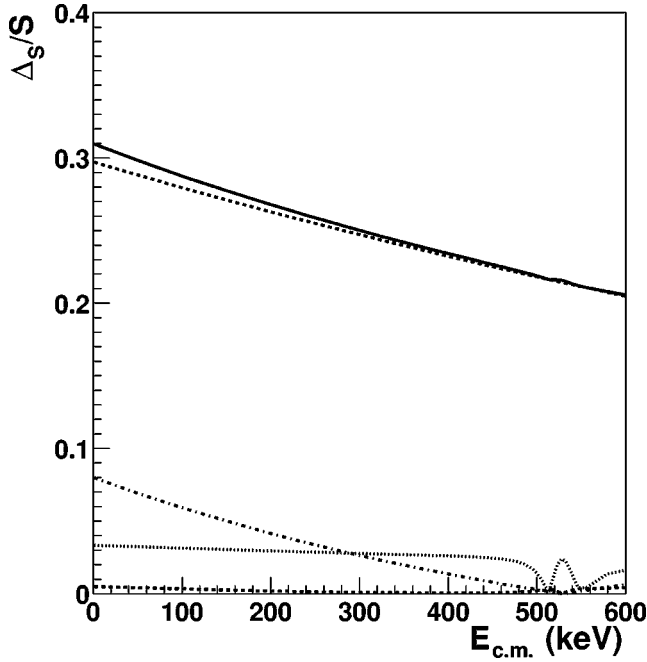
FIG. 10. Important contributions to the fractional uncertainty in the S factor. The uncertainty in the S factor due to Γ_γ of the resonance (dashed line), the ANC (upper dashed-dotted line), the total width of the resonance (dotted line), and the channel radius are shown (lower dashed line), together with the total uncertainty (solid line).

$=0.93$ eV$^{1/2}$. The first solution leads to destructive interference with the nonresonant component at energies below the resonance, but it yields a high internal radiative width $\left|[\Gamma_{\gamma J_f}^{J_i}(E_R^{c.m.})]_{int}\right| = 7.48$ eV. The second solution leads to constructive interference with the nonresonant component. This solution is favored based on microscopic calculations where it was shown that the internal and external parts of the $E1$ matrix elements have the same sign and very similar magnitudes. Note that an R-matrix approach similar to ours was also used by Barker [18] to infer the sign of the interference. However, neither the experimental radiative width nor the proton ANC for the ground state of ^{14}O were available at that time. The experimental radiative capture cross section for ^{13}C$(n,\gamma)^{14}$C with thermal neutrons and the spectroscopic factors from shell-model calculations and stripping reactions were used to estimate the internal and external matrix elements. Barker also found two solutions. His second solution resulted in a total radiative width of 3.85 eV, which is in excellent agreement with the experimental value, and was corroborated later by microscopic calculations with constructive interference [20].

As an additional check we used a simple single-particle model to analyze the dipole matrix element $\langle \varphi(r)|r|\psi(r)\rangle$, where $\varphi(r)$ and $\psi(r)$ are the $p + {}^{13}$N radial $1p_{1/2}$ bound-state and $s_{1/2}$ scattering wave functions. The latter is dominated by the $2s_{1/2}$ resonance at energies near E_R. This matrix element determines the radiative width. The behavior of the integrand for this matrix element is shown in Fig. 8. The resonant $2s_{1/2}$ scattering wave function has one node in the nuclear interior leading to the node in the integrand. The external and inter-

TABLE I. Reaction rate for ^{13}N$(p,\gamma)^{14}$O.

T_9	TAMU rate[error] (cm^3 s^{-1} mol^{-1})	NACRE rate (cm^3 s^{-1} mol^{-1})	TAMU/ NACRE
0.01	4.18×10^{-22}[30.2%]	2.01×10^{-22}	2.08
0.02	5.72×10^{-16}[30.1%]	2.78×10^{-16}	2.06
0.03	5.35×10^{-13}[30.0%]	2.63×10^{-13}	2.03
0.04	3.98×10^{-11}[29.8%]	1.99×10^{-11}	2.00
0.05	8.53×10^{-10}[29.7%]	4.34×10^{-10}	1.97
0.06	8.84×10^{-9}[29.6%]	4.58×10^{-9}	1.93
0.07	5.72×10^{-8}[29.4%]	3.02×10^{-8}	1.89
0.08	2.67×10^{-7}[29.3%]	1.44×10^{-7}	1.85
0.09	9.86×10^{-7}[29.1%]	5.43×10^{-7}	1.81
0.1	3.04×10^{-6}[29.0%]	1.71×10^{-6}	1.78
0.13	4.27×10^{-5}[28.5%]	2.56×10^{-5}	1.67
0.17	5.16×10^{-4}[27.8%]	3.34×10^{-4}	1.54
0.21	3.24×10^{-3}[27.0%]	2.22×10^{-3}	1.46
0.25	1.39×10^{-2}[26.3%]	9.85×10^{-3}	1.42
0.29	4.84×10^{-2}[25.6%]	3.47×10^{-2}	1.40
0.33	1.51×10^{-1}[24.9%]	1.11×10^{-1}	1.36
0.37	4.41×10^{-1}[24.3%]	3.41×10^{-1}	1.29
0.41	1.20×10^{0}[23.7%]	9.91×10^{-1}	1.21
0.45	2.98×10^{0}[23.2%]	2.60×10^{0}	1.15
0.49	6.69×10^{0}[22.8%]	6.09×10^{0}	1.10
0.53	1.36×10^{1}[22.5%]	1.28×10^{1}	1.06
0.57	2.54×10^{1}[22.2%]	2.44×10^{1}	1.04
0.61	4.38×10^{1}[22.0%]	4.27×10^{1}	1.03
0.65	7.09×10^{1}[21.9%]	6.99×10^{1}	1.02
0.69	1.09×10^{2}[21.8%]	1.08×10^{2}	1.01
0.73	1.58×10^{2}[21.8%]	1.58×10^{2}	1.00
0.77	2.22×10^{2}[21.8%]	2.22×10^{2}	1.00
0.81	2.99×10^{2}[21.8%]	3.01×10^{2}	1.00
0.85	3.92×10^{2}[21.9%]	3.95×10^{2}	0.99
0.89	5.00×10^{2}[21.9%]	5.04×10^{2}	0.99
0.93	6.23×10^{2}[21.8%]	6.30×10^{2}	0.99
0.97	7.59×10^{2}[21.7%]	7.70×10^{2}	0.99

nal parts have the same sign. To obtain destructive interference, the negative peak would need to be significantly larger than in the single-particle picture. We also calculated the radiative width using this simple single-particle model. Taking into account the relationship $(C_{p_{1/2}}^{^{14}O})^2 = S_{p_{1/2}} b_{p_{1/2}}^2$, where $S_{p_{1/2}}$ is the spectroscopic factor of the configuration $p + {}^{13}$N in the ^{14}O ground state, and $b_{p_{1/2}}$ is the single-particle ANC of the proton bound-state wave function, we can determine the spectroscopic factor. Using this spectroscopic factor, we fixed the normalization of the external matrix element to correctly match the experimental value of the proton ANC for the ^{14}O ground state. For a channel radius $a = 5$ fm, we find that $[\Gamma_{\gamma J_f}^{J_i}(E_R^{c.m.})]_{int}^{1/2} = 1.41$ eV$^{1/2}$ and $[\Gamma_{\gamma J_f}^{J_i}(E_R^{c.m.})]_{ext}^{1/2} = 0.95$ eV$^{1/2}$. Thus we find that in the single-particle approach the internal and external parts interfere constructively. Correspondingly, the total radiative width is $\left|\Gamma_{\gamma J_f}^{J_i}(E_R^{c.m.})\right|$
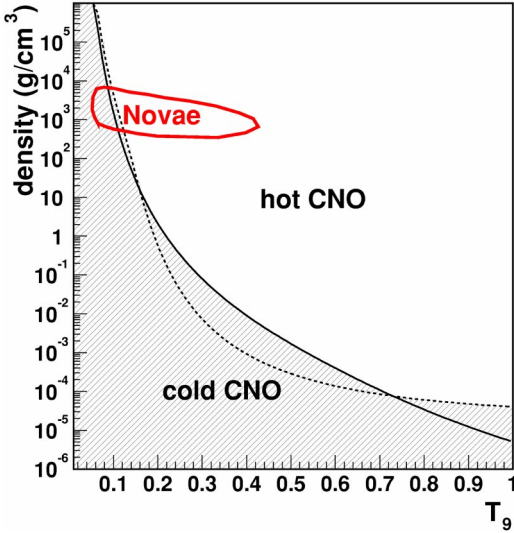
FIG. 11. (Color online) The updated density and temperature conditions for the transition from the cold to hot CNO cycle with a typical novae hydrogen mass fraction ($X_H = 0.77$). The solid line is the calculation with the competition between the $^{13}N(p,\gamma)^{14}O$ and the β decay of ^{14}O and ^{15}O with the updated reaction rates. The dashed line is the calculation with the competition between $^{14}N(p,\gamma)^{15}O$ and the β decay of ^{14}O and ^{15}O. The typical temperature and density condition for novae [1] is also shown as the circle in the upper left. For the typical novae temperature and density condition, $^{14}N(p,\gamma)^{15}O$ is slower than $^{13}N(p,\gamma)^{14}O$ and therefore controls the transition from the cold to hot CNO cycle.

=5.58 eV. This calculated single-particle radiative width is in excellent agreement with the updated single-particle microscopic calculations reported in Ref. [21]. We conclude that a simple single-particle model with the correct normalization of the tail and the spectroscopic factor determined from the ANC allows one to reproduce the microscopic single-particle radiative width, where the antisymmetrization effects in the nuclear interior have been properly taken into account. As expected, the single-particle radiative width exceeds the experimental value due to a high contribution from the nuclear interior. However, it has been shown in Ref. [21] that the inclusion of ^{13}N excited states decreases the internal matrix element, bringing the total radiative width into agreement with the experimental radiative width. While all these arguments are indirect, they strongly suggest that the internal part of the radiative width is that given by the second solution, which has the same sign as the channel part and consequently leads to constructive interference between the resonant and nonresonant terms.

The S factor calculated in the R-matrix approach is shown together with the result from Decrock *et al.* in Fig. 9. The relatively flat lower solid line, which is our result for direct capture alone, is about 30% larger than the result obtained by Decrock *et al.*, which is shown as the lowest dash-dotted line in Fig. 9. The two results just agree within the quoted uncertainties. At $E_{c.m.} = 140$ keV where the Gamow peak is located for $T_9 = 0.2$, our updated result using constructive interference, shown as the upper solid line, is about 38% higher than the previous result, which is shown as the upper dash-dotted line in Fig. 9. This is due to the larger direct capture contri-

bution from the ANC measurement. In Decrock's calculation, the resonance energy was taken to be 526 keV, which is smaller than Magnus's recommendation [17] ($E_R^{c.m.} = 527.9 \pm 1.7$ keV). Therefore, the peak of the resonance is shifted upward slightly to a higher resonance energy in our calculation. For completeness, we show the result that would be obtained with destructive interference as the dashed line in Fig. 9. The sign of interference can be easily checked with a direct measurement at high energy.

The uncertainties in the astrophysical S factor were investigated by varying the ANC for ^{14}O, Γ_γ, Γ_{total}, and $E_R^{c.m.}$ of the first resonance. Also the channel radius was varied from 4.5 fm to 5.5 fm. The uncertainty of $E_R^{c.m}$ only produces less than a 2% fluctuation for the S factor for energies less than 600 keV. The effects of all the other uncertainties on the astrophysical S factor are shown in Fig. 10. With increasing energy, the fractional uncertainty drops from 0.31 to 0.21. The uncertainty of the Γ_γ of the first resonance is the dominant component. The ANC and the total width of the first resonance also make significant contributions to the uncertainty for $E_{c.m.} < 0.6$ MeV.

VII. REACTION RATE Of $^{13}N(p,\gamma)^{14}O$

The astrophysical reaction rate [22] was calculated with

$$N_A\langle\sigma v\rangle_{NR} = N_A\left(\frac{8}{\pi\mu}\right)^{1/2}\left(\frac{1}{kT}\right)^{3/2}$$

$$\times \int_0^\infty S(E)e^{[-\sqrt{(E_G/E)}-(E/kT)]}dE, \qquad (5)$$

where N_A is Avogadro's number and E_G is the Gamow energy [22]. Based on the arguments given above, the S factor found for constructive interference was used to obtain the reaction rate.

The new reaction rates are listed in Table I together with NACRE's compilation. The new rates are about two times NACRE's compilation at lower temperature and are almost identical at higher temperature. The uncertainties, dominated by the error of the γ width of the first resonance, drop from 30% to 20% by varying the temperature from $T_9 = 0.01$ to $T_9 = 0.97$.

The new reaction rates were fit with NACRE's formula and are shown as the following:

$$N_A\langle\sigma v\rangle = \frac{4.02 \times 10^7}{T_9^{2/3}}\exp\left[-\frac{15.048}{T_9^{1/3}} - \left(\frac{T_9}{53.551}\right)^2\right]$$

$$\times (1 + 11.408T_9 - 20.296T_9^2 + 44.133T_9^3)$$

$$+ \frac{3.25 \times 10^5}{T_9^{2.838}}\exp\left(-\frac{6.470}{T_9}\right)cm^3\ s^{-1}\ mol^{-1}.$$

$$(6)$$

The overall fitting errors were less than 7% in a range from $T_9 = 0.01$ to $T_9 = 0.97$.

The updated density and temperature conditions for the transition from the cold to hot CNO cycle, with a typical nova hydrogen mass fraction ($X_H = 0.77$), are shown in Fig.

11. The reaction rate for $^{14}\text{N}(p,\gamma)^{15}\text{O}$ is slower than $^{13}\text{N}(p,\gamma)^{14}\text{O}$ when $T_9 < 0.16$ and $T_9 > 0.73$. For the typical novae temperature and density condition, the transition from the cold to hot CNO cycle is still governed by the competition between $^{14}\text{N}(p,\gamma)^{15}\text{O}$ and the β decay of ^{14}O and ^{15}O.

VIII. CONCLUSION

The dependence of the energy generation rate on the temperature changes dramatically for a transition from the cold to hot CNO cycle. A precise understanding to this transition process is vital to understand novae explosions. With the proton peripheral transfer reaction $^{14}\text{N}(^{13}\text{N},^{14}\text{O})^{13}\text{C}$, we have determined the ANC for $^{14}\text{O} \rightarrow ^{13}\text{N} + p$ and used this to update the nonresonant capture contribution to $^{13}\text{N}(p,\gamma)^{14}\text{O}$. Based on our results and other theoretical calculations, the S factor at low energy was calculated with constructive interference. With the updated reaction rate, a new density and temperature condition for the transition was determined.

[1] M. Wiescher, J. Gorres, and H. Schatz, J. Phys. G **25**, R133 (1999).

[2] M. S. Smith *et al.*, Phys. Rev. C **47**, 2740 (1993).

[3] C. Angulo, NACRE—Nuclear Astrophysics Compilation of REaction Rates, http://pntpm.ulb.ac.be/Nacre/ (2003).

[4] P. F. Bertone, A. E. Champagne, M. Boswell, C. Iliadis, S. E. Hale, V. Y. Hansper, and D. C. Powell, Phys. Rev. C **66**, 055804 (2002).

[5] A. M. Mukhamedzhanov, P. Bém, B. A. Brown, V. Burjan, C. A. Gagliardi, V. Kroha, J. Novák, F. M. Nunes, Š. Piskoř, F. Pirlepesov, E. Šimečková, R. E. Tribble, and J. Vincour, Phys. Rev. C **67**, 065804 (2003).

[6] P. Decrock *et al.*, Phys. Rev. C **48**, 2057 (1993).

[7] A. M. Mukhamedzhanov, C. A. Gagliardi, and R. E. Tribble, Phys. Rev. C **63**, 024612 (2001).

[8] X. Tang *et al.*, Phys. Rev. C **67**, 015804 (2003).

[9] A. Azhari, V. Burjan, F. Carstoiu, C. A. Gagliardi, V. Kroha, A. M. Mukhamedzhanov, F. M. Nunes, X. Tang, L. Trache, and R. E. Tribble, Phys. Rev. C **63**, 055803 (2001).

[10] James F. Ziegler, SRIM—the Stopping and Range of Ions in Matter, http://www.srim.org (2001).

[11] L. Trache, A. Azhari, H. L. Clark, C. A. Gagliardi, Y.-W. Lui, A. M. Mukhamedzhanov, R. E. Tribble, and F. Carstoiu, Phys. Rev. C **58**, 2715 (1998).

[12] L. Trache, A. Azhari, H. L. Clark, C. A. Gagliardi, Y.-W. Lui, A. M. Mukhamedzhanov, R. E. Tribble, and F. Carstoiu, Phys. Rev. C **61**, 024612 (2000).

[13] P. Bém, V. Burjan, V. Kroha, J. Novák, Š. Piskoř, E. Šimečková, J. Vincour, C. A. Gagliardi, A. M. Mukhamedzhanov, and R. E. Tribble, Phys. Rev. C **62**, 024320 (2000).

[14] A. M. Mukhamedzhanov, H. L. Clark, C. A. Gagliardi, Y.-W. Lui, L. Trache, R. E. Tribble, H. M. Xu, X. G. Zhou, V. Burjan, J. Cejpek, V. Kroha, and F. Carstoiu, Phys. Rev. C **56**, 1302 (1997).

[15] M. Rhoades-Brown, M. H. Macfarlane, and S. C. Pieper, Phys. Rev. C **21**, 2417 (1980); **21**, 2436 (1980).

[16] I. Thompson, Comput. Phys. Rep. **7**, 167 (1988).

[17] P. V. Magnus, E. G. Adelberger, and A. Garcia, Phys. Rev. C **49**, R1755 (1994).

[18] F. C. Barker, Aust. J. Phys. **38**, 657 (1985).

[19] F. C. Barker and T. Kajino, Aust. J. Phys. **44**, 369 (1991).

[20] P. Descouvemont and D. Baye, Nucl. Phys. **A500**, 155 (1989).

[21] P. Descouvemont, Nucl. Phys. **A646**, 261 (1999).

[22] C. Rolfs and W. Rodney, *Cauldrons in the Cosmos* (The University of Chicago Press, Chicago, 1988).